This document is confidential and is proprietary to the American Chemical Society and its authors. Do not copy or disclose without written permission. If you have received this item in error, notify the sender and delete all copies.

Ligand Structure Dependent Coherent Vibrational Wavepacket Dynamics in Pyrazolate-Bridged Pt(II) Dimers

Journal:	The Journal of Physical Chemistry
Manuscript ID	jp-2022-02256s.R2
Manuscript Type:	Special Issue Article
Date Submitted by the Author:	n/a
Complete List of Authors:	Kim, Tae Wu; Mokpo National University, Department of Chemistry Kim, Pyosang; Northwestern University, Chemistry Mills, Alexis; University of Washington, Department of Chemistry Chakraborty, Arnab; Virginia Tech, Kromer, Sarah; North Carolina State University at Raleigh, Chemistry Valentine, Andrew; University of Washington, Chemistry Castellano, Felix; North Carolina State University, Chemistry Li, Xiaosong; University of Washington, Department of Chemistry Chen, Lin; Argonne National Laboratory, Chemical Sciences and Engineering; Northwestern University, Department of Chemistry
Note: The following files were submitted by the author for peer review, but cannot be converted to PDF. You must view these files (e.g. movies) online.	
TOC_graphic.tif figure1.tif figure2.tif figure3.tif figure4.tif figure5.tif figure6.tif scheme1.tif	

SCHOLARONE™ Manuscripts

Ligand Structure Dependent Coherent Vibrational Wavepacket Dynamics in Pyrazolate-Bridged Pt(II) Dimers

Tae Wu Kim, ^{1,†} Pyosang Kim, ^{1,2} Alexis W. Mills, ³ Arnab Chakraborty, ⁴ Sarah Kromer, ⁴ Andrew J. S. Valentine, ³ Felix N. Castellano, ^{4,*} Xiaosong Li^{3,*} & Lin X. Chen^{1,2,*}

¹Chemical Science and Engineering Division, Argonne National Laboratory, Lemont, Illinois 60439, United States

²Department of Chemistry, Northwestern University, Evanston, Illinois 60208, United States

³Department of Chemistry, University of Washington, Seattle, Washington 98195, United States

⁴Department of Chemistry, North Carolina State University, Raleigh, North Carolina 27695-8204, United States

Corresponding Author

*Lin X. Chen: lchen@anl.gov, l-chen@northwestern.edu, Xiaosong Li: xsli@uw.edu, Felix N. Castellano: fncastel@ncsu.edu

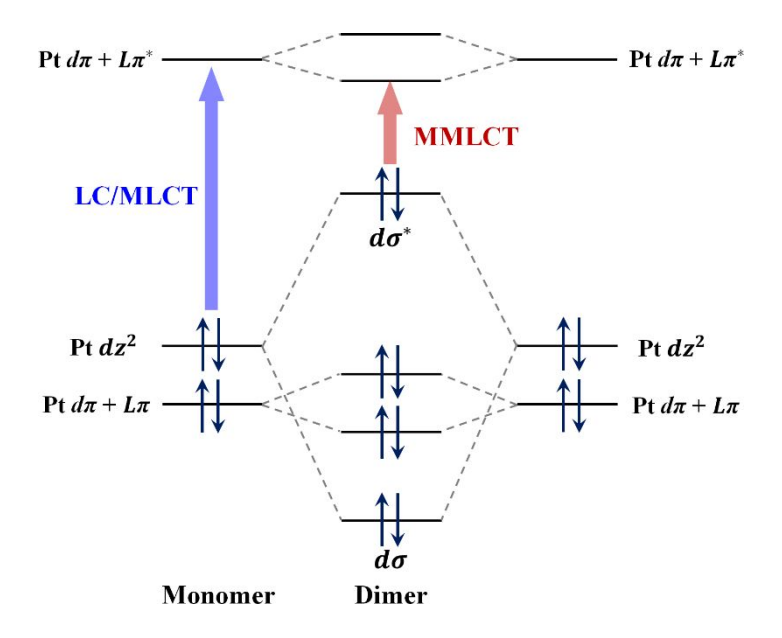
Abstract

Bimetallic transition metal complexes have gained increasing attention because of their versatile functions in solar energy conversion and photonics applications arising from intermetal electronic coupling. In bimetallic platinum (Pt) complexes, electronic communication between the Pt-centered and ligand-centered moieties have been shown to be critical for defining their excited-state dynamic trajectories undergoing either localized ligand centered (LC)/metal-to-ligand-charge-transfer (MLCT) transitions or delocalized metal-metal-toligand-charge-transfer (MMLCT) transitions. The branching of the excited-state intersystem crossing (ISC) trajectories are modulated through structural factors that alter the relative energies of the different states. In this study, we investigated the correlation of the structural factors influencing the excited state trajectories. Using femtosecond broadband transient absorption (fs-BBTA) spectroscopy, ultrafast dynamics in the excited state of two select Pt(II) dimers have been mapped out using their coherent vibrational wavepacket signatures in corresponding transient absorption spectra. To examine how the ligand moieties of the Pt(II) dimers influence excited-state dynamics and the coherent vibrational wavepacket behavior, we carried out comparative studies on two pyrazolate-bridged Pt(II) dimers of the general formula $[Pt(^tBu_2Pz)(N^{\wedge}C)]_2$ ($^tBu_2Pz = 3.5$ -di-tert-butylpyrazole); $N^{\wedge}C = 7.8$ -benzoquinoline (bzq. 1) or 1-phenylisoquinoline (piq, 2)). We found that photoexcitation into the low energy absorption bands of 1 and 2 respectively induce the formation of ¹MMLCT states from which ultrafast ISC proceeds, resulting in stimulated emission quenching and decoherence of the vibrational wavepacket motions. The results obtained in this study suggest that both energetics and the structural rigidity of the aromatic cyclometalating ligands in 1 and 2 can significantly influence dynamics along the excited state trajectory characterized by dephasing of the coherent oscillations. The collective results provide direct evidence of how ligand structure alters electronic dynamics along excited state trajectories associated with ISC processes, providing insight into using ligand design to steer photochemical processes.

Introduction

Bimetallic transition metal complexes (TMCs) bridged by organic ligands have gained attention due to their potential applications as photocatalysts, 1-3 light-emitting materials, 4,5 and photoluminescent sensors.^{6,7} Among the various types of bimetallic TMCs, Pt(II) dimers have been considered as promising light-emitting materials due to their long-lived phosphorescence and high emission quantum yields.⁸⁻¹¹ Pt(II) dimers constructed from pyrazolate bridges and conjugated aromatic cyclometalating (CM) ligands feature metal-metal d⁸-d⁸ interactions displaying prominent absorption and emission properties that depend on the Pt–Pt distance. 12-¹⁴ Previous studies of CM Pt(II) dimers with sufficiently short Pt–Pt distances (< 2.95 Å) produce metal-metal-to-ligand-charge-transfer (MMLCT) excited states upon photoexcitation into the lowest energy visible absorption bands. 12,15-19 This MMLCT transition predominantly promotes an electron from the HOMO (mainly Pt(5 d_{z^2})-Pt(5 d_{z^2}) d σ^*) to LUMO (mainly N^C ligand-centered π^*), which depletes electron density in the antibonding orbital of $d\sigma^*$, resulting in an increase of the Pt-Pt bond order by ~0.5, contracting the Pt-Pt distance as shown in Scheme 1. Due to this photoinduced charge transfer and its subsequent electronic dynamics related to the associated structural rearrangement, some of these Pt(II) dimers have been extensively studied through various spectroscopic and theoretical approaches. 15-24

Scheme 1. Representative energy-level diagram illustrating the metal-metal interactions in pyrazolate bridged Pt(II) dimers. The metal-metal-to-ligand-charge-transfer (MMLCT) transition (red arrow) leads to a decrease of antibonding orbital ($d\sigma^*$), resulting in an increase of the Pt–Pt bond order.



Previous studies using femtosecond transient absorption (TA) spectroscopy show that these Pt(II) dimers display characteristic coherent vibrational wavepacket (CVWP) motion, on the excited state potential energy surfaces (PESs) on ultrafast time scales. 19,21,22 This originates from the superposition of vibrational manifolds in the initially-populated excited state, 25-28 which is in stark contrast to the electronic (or vibronic) coherences arising from coherent excitations of multiple excited states.²⁹⁻³⁴ Earlier studies describing the vibrational coherence in a pyrazolate-bridged Pt(II) dimer of $[Pt(ppy)(\mu^{-t}Bu_2Pz)]_2$, or Pt-ppy, identified that the observed coherent vibrational wave packet (CVWP) motions were associated with the Pt-Pt stretching mode. 17,21 A recent study using the combination of fluorescence up-conversion and TA spectroscopies further supported these original findings where the dephasing of the Pt-Pt vibrational modes was associated with fluorescence quenching during the ISC process, and structural flexibility might be a mitigating factor for the regulation of vibrational coherence.¹⁹ Despite these experimental efforts, the exact role of the nature of the ligand moiety in view of vibrational coherence phenomena and its dynamic behavior has not been fully elucidated to date. Furthermore, most spectroscopic studies interrogating pyrazolate-bridged Pt(II) dimers have primarily focused on the vibrations related to the Pt-Pt stretching mode due to limited temporal resolution and the available probing spectral bandwidth.

In this study, we investigated the ultrafast dynamics of two newly conceived pyrazolatebridged Pt(II) dimers $[Pt(^tBu_2Pz)(N^{C})]_2$, where $^tBu_2Pz = 3,5$ -di-tert-butylpyrazole), N^C is 7,8-benzoquinoline (bzq, 1) or 1-phenylisoquinoline (piq, 2). The vibrational coherence formed in the excited state of these molecules was interrogated using a femtosecond broadband transient absorption (fs-BBTA) setup developed recently in our laboratory, featuring an extended probing spectral range with improved temporal resolution to ~25 fs. In particular, the influence of the CM (C^N) ligand moiety on the resultant excited-state dynamics and CVWP behavior were investigated in 1 and 2 (Figure 1).¹² By performing global kinetic analyses, we found that photoexcitation into the lowest energy absorption band in 1 and 2 induced ultrafast ISC from the emissive singlet (¹MMLCT, or S₁) state to its corresponding triplet excited state (3MMLCT or T₁), from which relaxation towards the ground state proceeded. Based on normal mode analyses, the CVWP motions observed in the ¹MMLCT state in 1 and 2 are associated mainly with two reaction coordinates: the torsional motions of the bzq (1) and piq (2) ligand moieties and the Pt-Pt stretching, along with the ultrafast ISC trajectories. Comparison of the current results to other recent studies on $[Pt(^tBu_2Pz)(ppy)]_2$ (ppy = 2-phenylpyridine, 3)^{19,21} suggests that the electronic and nuclear structural factors of the CM ligand of the Pt-Pt core in 1 and 2 markedly affects the CVWP dephasing dynamics that was linked to structural changes in the excited state. Our study yields direct evidence of how the molecular structure of the C^N ligands, related to the conformational flexibility in the bimetallic complexes, alters the dynamics of vibrational coherence during the ISC processes.

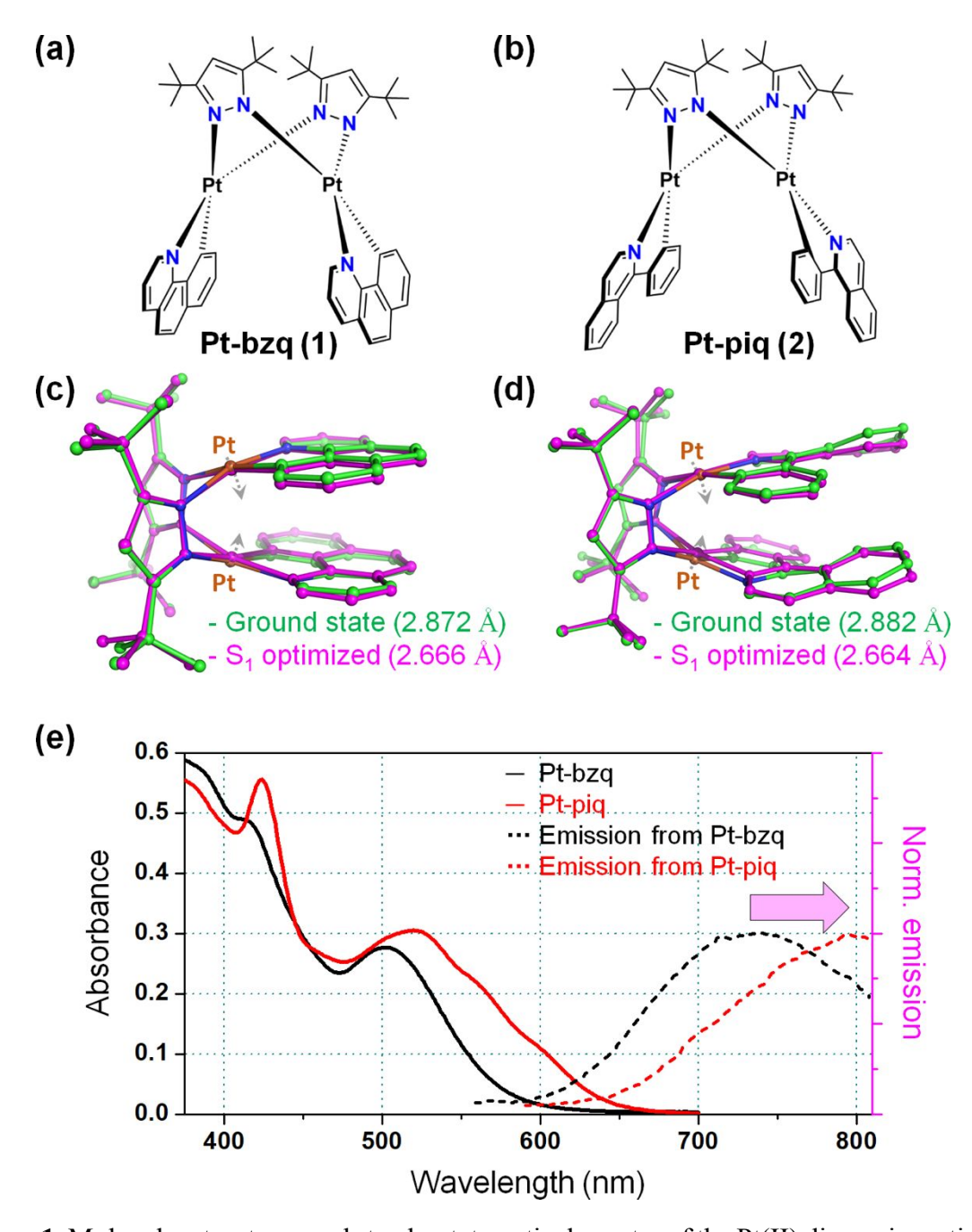


Figure 1. Molecular structures and steady-state optical spectra of the Pt(II) dimers investigated in this study. Molecular structures of (a) $[Pt(bzq)(\mu^{-t}Bu_2Pz)]_2$, named as Pt-bzq or 1, and (b) the trans isomer of $[Pt(1-piq)(\mu^{-t}Bu_2Pz)]_2$, named as Pt-piq or 2. Three-dimensional molecular

structures of (c) Pt-bzq and (d) Pt-piq optimized from the DFT calculations. The values of Pt—Pt distances in the optimized structures are in parentheses. The transition from the ground state to the lowest singly-excited state (S₁) accompanies the decrease of Pt-Pt distance in the Pt(II) dimers, indicated by the gray arrows. (e) Absorption spectra (solid lines) and emission spectra (dotted lines) of Pt-bzq and Pt-piq dissolved in THF.

Experimental Section

Sample Preparation. [Pt(bzq)(μ - t Bu₂Pz)]₂ and [Pt(piq)(μ - t Bu₂Pz)]₂ were prepared by slight modifications of previously established procedures with all relevant details and structural characterization provided as Supporting Information and Figures S1–S4.¹² All the chemicals required for the synthesis of **1** and **2** were purchased from commercial sources and were used without further purification.

Steady-state Spectroscopic Measurements. Linear absorption spectra for the Pt(II) dimers were acquired using a Shimadzu UV-3600 spectrometer. Steady-state photoluminescence emission spectra were acquired using a Photon Technologies International model QM-2 spectrofluorometer. All the samples were dissolved in THF and measured at room temperature.

Femtosecond Broadband Transient Absorption Spectroscopy (fs-BBTA). Fs-BBTA spectra were measured with femtosecond laser pulses using a visible pump–broadband probe scheme. The output pulses at 1030 nm from a Yb:KGW based regenerative amplifier (Light conversion Pharos-10W, 200 fs, 10 kHz repetition rate) were split into pump and probe beams. On the pump arm, the 1030 nm laser pulses were converted using second harmonic generation into the pump pulses centered at 560 nm, equal to 17857 cm⁻¹, with a bandwidth of 2132 cm⁻¹ using a homebuilt, all-reflective-optical non-collinear optical parametric amplifier (NOPA) based on third harmonic generation pumping (THG-NOPA). The pump pulses were sent through a pair of chirped mirrors (Layertec) in combination with a pair of fused silica wedges in order to pre-compensate for the dispersion obtained from transmissive optics and were compressed to near-transform-limited pulses at the sample position. As shown in Figure S5, the pulse duration of the compressed THG-NOPA output was approximately 24.7 fs, which was characterized from the second-harmonic-generation frequency-resolved optical gating (SHG-FROG) equipped with a 10 μm BBO crystal (Newlight Photonics Inc.). On the probe arm, the 1030 nm laser pulses were sent into a *c*-cut sapphire window of 2 mm thickness and

converted into a white light continuum spanning from the visible to near-infrared (NIR) region by self-phase modulation. The visible-to-near infrared portion (540–820 nm) of the white light continuum was compressed by a pair of chirped mirrors (Laser Quantum). The white light continuum was compressed to near-transform-limited regime and was used as broadband probe pulses. The probe pulses were time-delayed with respect to the pump pulses using a motorized linear stage (Newport, XMS160-S). By recording "pump-on" and "pump-off" probe spectra, the differential absorption (ΔA) spectrum was obtained as a function of time. The spectrum of the transient signal and the reference were detected by a spectrometer (Andor, Kymera 328i) equipped with a sCMOS camera (Andor, Zvla-5.5). In all measurements, the polarization direction of the pump pulses was set to be at a magic angle (54.7°) relative to that of the probe in order to prevent polarization-dependent signals. From impulsive stimulated Raman scattering measurements of neat solvents, tetrahydrofuran (THF) and acetonitrile (ACN), the instrumental response function of the TA measurement was determined to be ~30 fs at the sample position. For the fs-BBTA measurement, the absorbance of sample stored in the 1-mm path quartz cuvette was set to be less than 0.3 at the excitation wavelength region. The excitation energy was set to 100 nJ/pulse at the sample position. In order to check the sample integrity, the absorption spectra of samples were measured before and after the TA measurements, which did not show any evidence of sample degradation.

Quantum Chemical Calculations. All the density functional theory (DFT) calculations were implemented at University of Washington by using the Gaussian 16 package.³⁵ For the optimization of molecular geometries, we employed ω B97X-D functional, and used the basis sets of 6-31G(d) for all light atoms and LanL2DZ with an effective core potential for the Pt atoms. The ω B97X-D functional was chosen because it is range-separated, to better describe charge-transfer excited states,³⁶ and it contains dispersion corrections, necessary to capture π - π interactions.³⁷ The characters of excited states in the Pt(II) dimers were estimated by using time-dependent density functional theory (TD-DFT). Energetic minima found by the optimized structures of ground- and excited-state were confirmed by the normal mode calculations at the same level of theory. To generate potential energy surfaces (PESs), the single-point TD-DFT calculations were performed at the intermediate structures reconstructed from the linear interpolation of the ground-state and the singlet and triplet MMLCT geometries for each complex.

Results and Discussion

Ground State Absorption and Emission Spectra. The linear absorption and emission spectra of 1 and 2 measured in THF are presented in Figures 1 and S6. The Pt-bzq complex 1 displays a strong absorption band below 350 nm, an intermediate absorption band around 420 nm, and a weak absorption band above 500 nm. According to the previous studies of cyclometalated pyrazolate-bridged Pt(II) dimers with identical core framework, ¹² the optical absorption below 350 nm is assigned as the ligand-centered (LC) electronic transitions, the absorption around 450 nm to metal-to-ligand charge transfer (MLCT) transitions, and the absorption above 500 nm to metal-metal-to-ligand charge transfer (MMLCT) transitions. The LC and MLCT transitions are localized on one half of the pseudo-two-fold symmetric molecule, whereas the MMLCT transition is delocalized, originating from the electronic transition of a Pt-Pt centered σ^* orbital to a N^C ligand-centered π^* orbital. The MMLCT transition depletes electron density from the antibonding σ^* orbital thereby increasing the Pt-Pt bond order by 0.5, resulting in a contraction of the Pt-Pt distance. The spectral feature of lowest energy absorption band in 2 containing the piq CM ligands is red-shifted from that of 1. The emission spectrum of 1 showed a prominent emission peak near 740 nm, while the emission peak in 2 was further red-shifted. Based on a previous study, 12 these emission features are consistent with decay from 3MMLCT excited states.

Structures of the Ground and MMLCT States from Quantum Mechanical Calculations.

To gain insight into the molecular structures and electronic interactions in the ground and excited states of **1** and **2**, we conducted geometry optimization using DFT and TDDFT methods. Based on the optimized structures of the ground state (S_0) and the lowest singlet state (S_1), we also calculated vibrational modes and their corresponding frequencies. As shown in Figure 1, the optimized molecular structure in the S_1 state shows a decrease of Pt–Pt distance relative to that in the S_0 state, independent of the CM ligands. Specifically, the Pt–Pt distance in the ground state of **1** is 2.872 Å and it shortens to 2.666 Å in the S_1 state, giving a Pt–Pt distance change (ΔR_{Pt-Pt}) of 0.206 Å. Such a Pt–Pt distance shortening similarly occurs in **2** with $\Delta R_{Pt-Pt} = 0.218$ Å, from the Pt–Pt distance of 2.882 Å in the S_0 state to 2.664 Å of the S_1 state. The other notable structural feature difference between **1** and **2** is the magnitude of the ligand distortions, the former much smaller than the latter, showing the ligand flexibility. According to the results from the TDDFT calculations summarized in Table S1, the TDDFT calculations overestimated the energy values corresponding to the lowest electronic transition relative to

the experimental ones. This features were commonly observed in the previous studies about the TDDFT calculations of Pt-complexes due to the self-interaction error arising from the electron transfer in the CT state. 19,38 Nevertheless, the lowest energy electronic transition, S₀ \rightarrow S₁, appearing in the ground state absorption spectrum in 1 is dominated by the HOMO-LUMO transition. To clearly show the charge distribution in 1, we present the natural transition orbitals (NTOs) derived from the combination of particle-hole transitions corresponding to the optical absorption in the spectral region, which helps to identify the origins of the electronic transitions.³⁹ For the lowest electronic transition in 1 summarized in Table S1, the charge density of the hole in the NTOs is localized around the metal-centered moieties, and the charge density of the electron in NTOs is delocalized from the metal-centered to the bzq ligand moieties. According to the NTOs of 2 summarized in Table S2, the lowest energy transition, $S_0 \to S_1$, is also dominated by the HOMO-LUMO transition, moving electron density from the metal center to the piq ligands. The electronic behavior in the NTOs of Pt-piq resembles that in Pt-bzq. The behavior of charge density in view of the calculated NTOs clearly exhibits the transfer of charge between the metal-centered and the ligand moieties, supporting the common occurrence of MMLCT transitions in 1 and 2. Meanwhile, the calculated excitation energy, corresponding to the transition of $S_0 \rightarrow S_1$ in 2, shows a significant spectral red-shift compared with that in 1. This spectral feature in 2 likely originates from larger π -conjugation with a total of 15 C and N atoms in pig, compared with 13 C and N atoms in bzq, and the enhanced interaction between the two parallel-aligned ligands, linked to a π - π interaction. 12,15,40

Excited State Dynamics Probed by fs-BBTA Spectroscopy. To explore the excited state dynamics, we performed fs-BBTA measurements for 1 and 2 dissolved in tetrahydrofuran (THF). The laser pulse centered at 560 nm with a bandwidth of 66 nm full-width-at halfmaximum (FWHM) was used as the pump pulse (Figure S6). According to the spectral overlap between the absorption spectra and the excitation profile (Figure S6), the photoexcitation condition is predominantly resonant with the lowest absorption peak (500-600 nm) assigned as MMLCT transitions, as supported by the results from the TDDFT calculations. The TA spectra of 1 and 2 display not only the features associated with the ground-state bleach (GSB), stimulated emission (SE), and excited state absorption (ESA), but also temporal oscillatory modulations superimposed on these features, presumably due to CVWP motions. To

disentangle the kinetics extracted from the excited state optical signatures from the overlaid oscillatory signals, we applied global kinetic analysis to these TA spectra. The details of the global kinetic analysis based on singular value decomposition (SVD)⁴¹ are described in the SI. According to the global kinetic analysis shown in Figure S7, the spectrally distinct three species and two time constants were observed in the primary photoreactions of 1 and 2, and thus this result suggest the sequential kinetic model such as $S_1 \rightarrow T_1 \rightarrow$ relaxed T_1 . The spectral features of each excited state species and its conversion kinetics are described using species-associated difference spectra (SADS) and the time constants, respectively, under the assumption of a sequential kinetic model. Although the sequential kinetics were employed for the interpretation of electronic dynamics, we cannot completely rule out the presences of the branching pathways associated with the relaxation from the initially excited state.

In 1, the conversions of SADS1 to SADS2 and subsequent SADS2 to SADS3 occur with time constants of 0.236 (± 0.016) and 1.76 (± 0.50) ps, respectively. The decay time constant of SADS3 to a long-lived species cannot be determined due to the limited delay time window available. Thus, additional TA measurements were carried out using a probe delay time window up to 130 ps (Figure S8), which showed that the amplitude of SADS3 only decays less than 10%, as expected for similar pyrazolate-bridged Pt(II) dimers having triplet MMLCT lifetimes of hundreds of nanoseconds. ^{12,15} SADS1 displays the prominent SE signal at 625–775 nm with the negative peak centered around 700 nm and the ESA signal below 625 nm. According to the steady-state absorption and emission spectra of 1, the onset of the absorption spectrum occurs near 650 nm and the emission peak is located around 745 nm. In this regard, the SE feature with the negative signal is likely to be spectrally blue-shifted than the steadystate emission from the ³MMLCT state, and thus can be assigned as the emission from the initially populated singlet excited state. The transition of SADS1 to SADS2 with the time constant of 236 fs accompanies the quenching of SE feature in the concurrence of the growth of ESA feature at 600-820 nm. Such a spectral change involving the quenching of the SE feature suggests that the singlet excited state is converted to a non-emissive excited state. Subsequently, the newly-formed ESA feature in SADS2 further grows in the SADS3 with a prominent positive peak at 650 nm.

In 2, the corresponding transitions among the excited states were determined to occur with time constants of 255 (\pm 13) fs and 2.85 (\pm 0.54) ps, respectively. Based on the decay profile for the 130-ps-long delay time window shown in Figure S8, the final state corresponding to the

SADS3 shows the slow recovery toward the ground state, which is like that in 1. SADS1 shows a broad ESA feature across the entire probing region, but there is a valley feature in the spectral window from 650 nm to 820 nm. According to the steady-state absorption and emission spectra of 2, the onset of the absorption spectrum occurs at 670 nm and the emission peak is located around 800 nm. Comparing the spectral position of the dip at 750 nm with the emission peak at 800 nm, we can infer that the valley shape originates from the spectral overlap with the ESA and SE features arising from the initially populated singlet excited state. In the transition from SADS1 to SADS2, this valley shape disappears and converts to a broad ESA feature with a peak at 660 nm. Thus, this transition having a time constant of 255 fs can be assigned as the transition of the singlet excited state to the non-emissive excited state, which is highly comparable to that observed in Pt-bzq. The newly formed ESA feature as well as the GSB feature further evolves in SADS3.

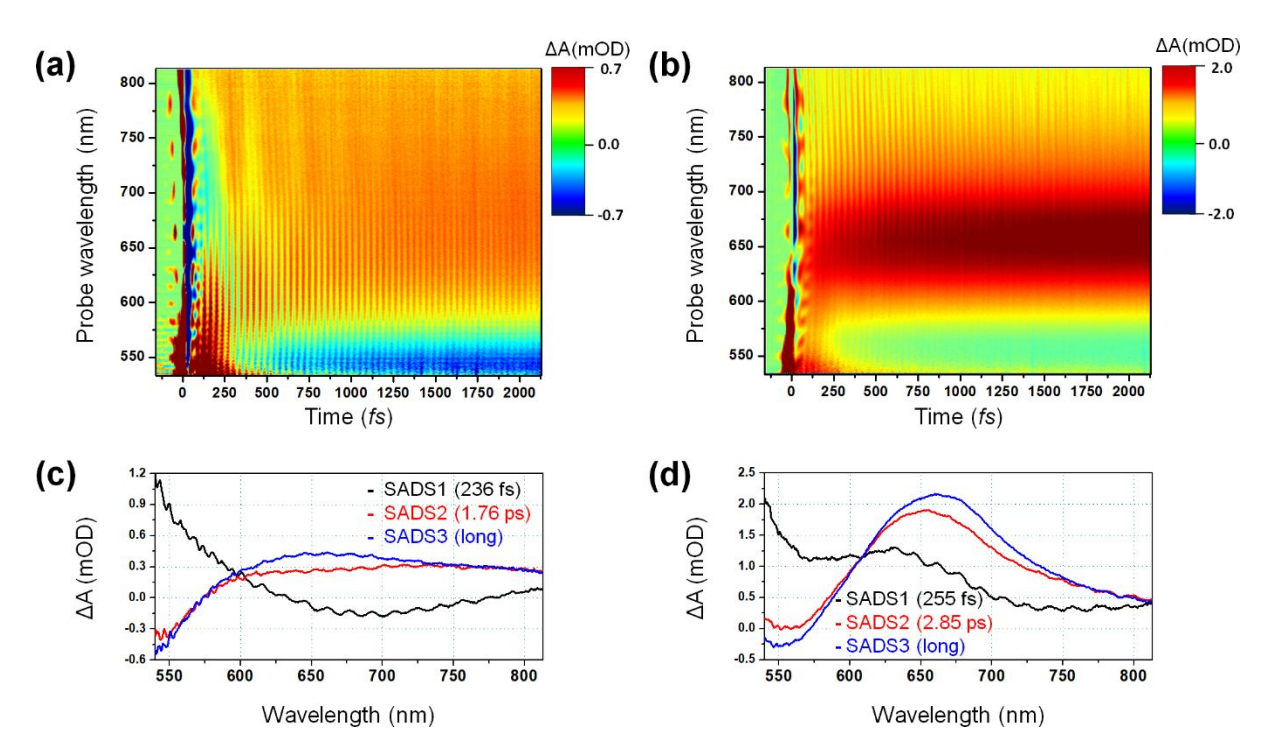


Figure 2. Femtosecond transient absorption (fs-TA) spectra. Raw TA spectra of (a) Pt-bzq and (b) Pt-piq. Species-associated difference spectra and those decay constants of (c) Pt-bzq and (d) Pt-piq determined from the global kinetics analysis of TA spectra. For the TA measurement, all the samples were dissolved in THF.

Both Pt-bzq and Pt-piq complexes have a SE feature in the SADS1 that disappears due

to the transition to SADS2 with a time constant of ~200 fs. The quenching dynamics of the SE feature is therefore assigned as the process of intersystem crossing (ISC) from ¹MMLCT to ³MMLCT. These observations can be linked to the results from previous fluorescence upconversion measurements on the analogous Pt-ppy complex, or 3.19 We note that the onset of the absorption spectrum in 3 originates near 620 nm due to a smaller degree of π -conjugation in the ppy ligands with respect to those in Pt-bzq and Pt-piq. Accordingly, the red-shift observed in the SE signals of Pt-bzq and Pt-piq can be attributed to the increased π -conjugation in those ligands. For Pt-ppy, we additionally performed a benchmark calculation by employing the exact same level of TDDFT used in the calculations of Pt-bzq and Pt-piq. The results from the TDDFT calculation, summarized in Table S3, clearly indicated that the smaller π conjugated ppy ligands give rise to a higher π^* MO energy and thus the spectral blue-shift in the transition of $S_0 \rightarrow S_1$, dominant by the HOMO to LUMO transition, comparing with Pt-bzq and Pt-piq. It is notable that the SE signal in 1 is more intense than that in 2 (Figure 2 SADS results) although their time constants for the SADS1 to SADS2 conversion are similar. During the first a few ps of the excitation, the rates of the IC processes in Pt-bzq and Pt-piq within the triplet manifold are comparable to the same process in relaxation processes, as observed in related pyrazolate-bridged Pt(II) dimers. 15,16 In Pt-pig, the relaxation of SADS2 with a time constant of 2.85 ps was slightly delayed relative to that seen in Pt-bzq (1.76 ps). Nevertheless, the spectral change from SADS2 to SADS3 was similar with that in Pt-bzq, implying that the transition of SADS2 to SADS3 involves the relaxation of the MMLCT triplet excited state.

Coherent Wavepacket Dynamics and Their Implications to the Excited State Trajectories.

The fs-BBTA spectra of 1 and 2 shown in Figure 2 exhibit temporal oscillations superimposed on the population dynamics of their requisite excited states. To extract pure temporal oscillations, we subtracted the excited-state population dynamics, determined from global kinetic analysis, from the total TA signals. The oscillation signals found in the residuals after these subtractions were Fourier transformed to extract the wavelength-dependent Fourier transform power spectra (FTPS) presented in Figure 3. Although the excitation pulse centered at 560 nm from the THG-NOPA is solely resonant with the electronic transitions of 1 and 2, the THF solvent still presents off-resonant signals, induced from the impulsive stimulated Raman (ISR) process, which were independently generated from neat THF using optical heterodyne-detected birefringence⁴² (Figure S9). The FTPS of the pure THF solvent shows a

narrow peak at 917 cm⁻¹, while the low-frequency region below 800 cm⁻¹ is free from the off-resonant responses of this solvent. The frequency of 917 cm⁻¹ observed in the FTPS of THF is quantitatively similar to the vibrational frequency of 914 cm⁻¹, reported from Raman spectroscopy, thus, the peak can be assigned to the breathing motion of the furan ring.⁴³

In the low-frequency region below 800 cm⁻¹, the FTPS for Pt-bzq displays prominent vibrational frequencies of 22, 115, and 132 cm⁻¹ at the probe wavelength of 560 nm. Among those frequencies, 132 cm⁻¹ is also observed at probe wavelengths of 620 and 720 nm (with a very slightly shift to 137 cm⁻¹) shown in Figure 3c. Considering the experimental frequency resolution of ~5 cm⁻¹, the two peaks of 132 and 137 cm⁻¹ are indistinguishable from one another. The time-dependent oscillatory residual profiles at probe wavelengths of 560, 620, and 720 nm are given in Figure 4. Although the oscillatory signals at the 560 nm probe wavelength clearly

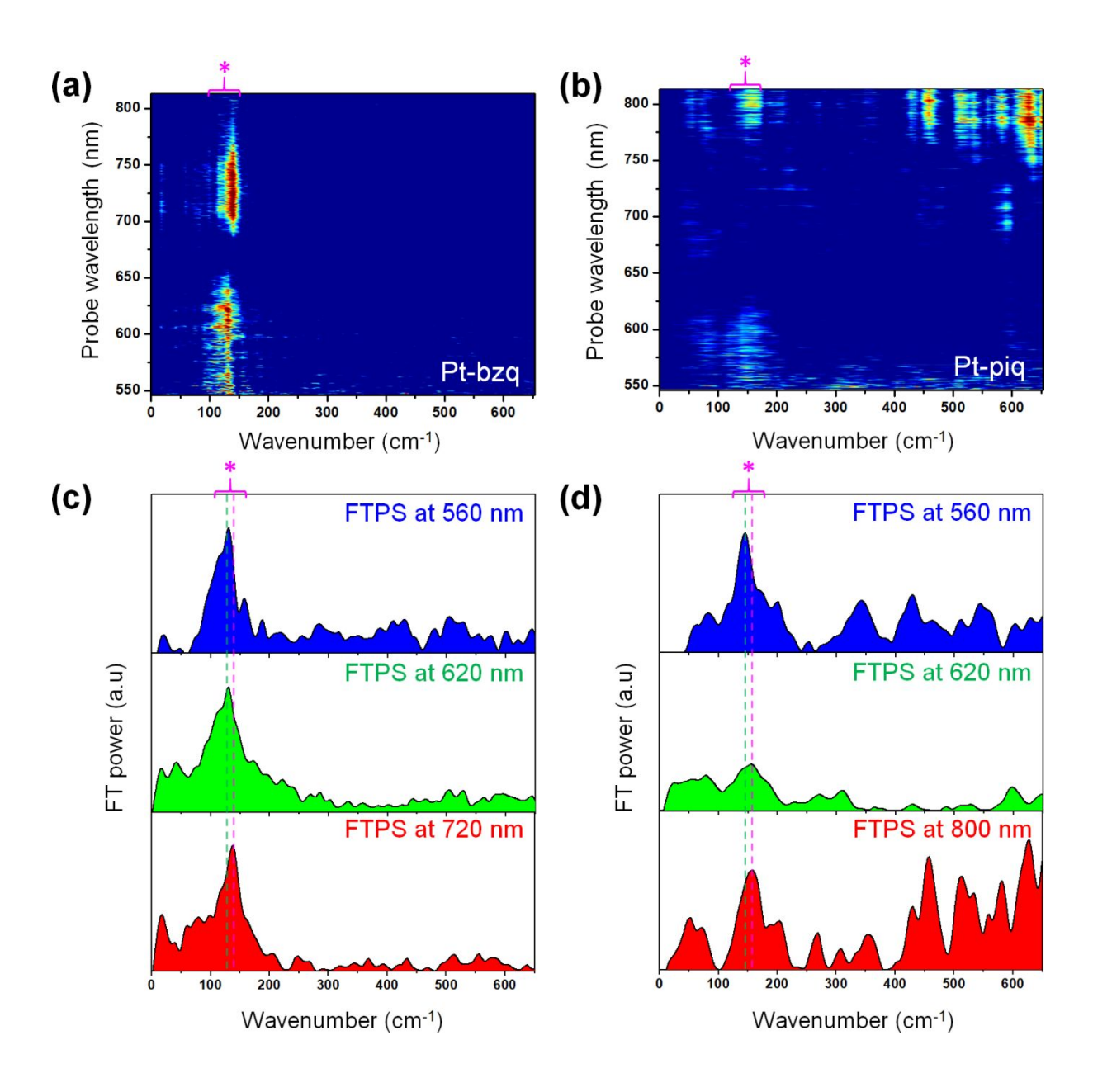


Figure 3. Wavelength-resolved Fourier transform power spectra (FTPS). Wavelength-resolved FTPS of (a) Pt-bzq and (b) Pt-piq with the probe spectral window of 540 - 810 nm. (c) FTPS of Pt-bzq at the selected probe wavelengths. (d) FTPS of Pt-piq at the selected probe wavelengths. In the FTPS of Pt-bzq and Pt-piq, the prominent peaks around 130 cm⁻¹ were labeled by asterisks.

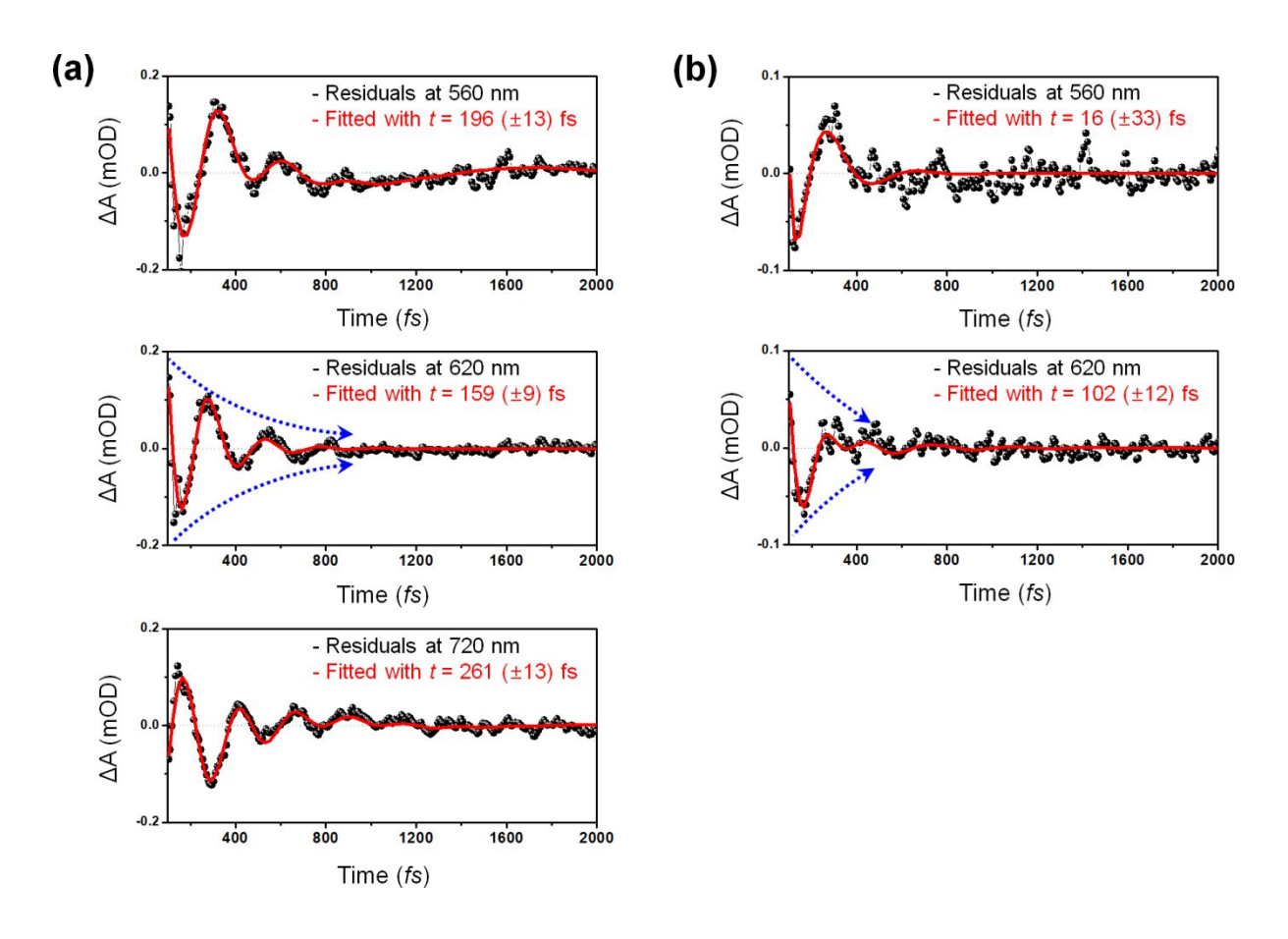


Figure 4. Oscillatory components obtained by subtracting the electronic population dynamics from the fs-TA data. Oscillatory components (black circles) of (a) Pt-bzq and (b) Pt-piq at the selected probe wavelengths. The oscillation components were fitted by the damping cosine functions (red lines), whose damping constant is given at the top right. In Pt-piq, the damping of coherent oscillations is much faster than in Pt-bzq.

possess a lower frequency than that observed at 620 and 720 nm, its initial phase is synchronized with that measured at 620 nm. In contrast, the oscillations at 720 nm are ~180° out-of-phase from those at 560 and 620 nm. To determine the dephasing times of the CVWP, we performed sinusoidal fitting using the observed frequencies with their corresponding damping time constants. Accordingly, fitting the 620 nm data generated a frequency of 132 cm⁻¹, corresponding to the temporal period of ~250 fs, which undergoes dephasing with a damping time constant of ~159 fs. At the probe wavelength of 720 nm, the frequency of 137 cm⁻¹, corresponding to the temporal period of ~243 fs, is dephasing with a time constant of ~261 fs. As shown in Figures 3b and 3d, the FTPS of 2 shows prominent vibrational frequencies of 83 and 140 cm⁻¹ at the probe wavelength of 560 nm, but the frequency bandwidths are much broader than those in 1. Among these frequencies, 140 cm⁻¹ is slightly shifted to 160 cm⁻¹ at 620 nm. The residual profiles shown in Figure 4b indicate that the temporal oscillations at the probe wavelengths of 560 and 620 nm have a common initial phase, similar to 1. However, the oscillation amplitudes in 2 were damped much more quickly compared to those in 1, which made the frequency distribution much broader. The CVWP dephasing times from these oscillatory signals are even shorter than a full vibrational period. Nevertheless, the frequencies of 140 (560 nm) and 160 cm⁻¹ (620 nm), corresponding to the temporal periods of ~238 and ~208 fs, and they dampen so fast that the dephasing time is hard to characterize.

The dephasing time for 1 is comparable to that of the SADS1 to SADS2 transition (236 fs), while that for 2 precedes the initial transition with a time constant of 255 fs. In this case, the dynamic behaviors of the vibrational coherences are likely associated with that of the initially formed singlet excited state, S₁ having the Franck-Condon (FC) geometry, which is then is likely to undergo dephasing during the ultrafast transition related to the ISC process. Comparing the spectral shapes of SADS1 and FTPS in 1, the short-lived oscillations of 132 and 137 cm⁻¹ were observed in the probe region covering 570 to 820 nm whereas the transient signals in SADS1 mainly originates from ESA and SE. Meanwhile, the wavelength-dependent residual map for 1 presented in Figure S10 indicates that the spectral position of a distinct nodal point around 675 nm along the axis of the probe wavelength was located outside of the ground-state absorption region. The existence of nodal point as a function of time delay can be interpreted as two possible dynamics; i) The overlap of ground and excited state coherences occurs in the ultrafast time regime and the phase of excited state coherence is flipped by 180° compared to that of ground state coherence. 41,44-46 ii) The ground-state or excited-state wavepacket moves back and forth on either side of potential energy surface as a function of its

normal coordinate, resulting in a phase change of the beatings at a probe wavelength corresponding to the equilibrium of the potential energy curve. Thus, the spectral position of the node can be a strong indication of the origin of the CVWP motion; the ground-state coherence produces the nodal point around the absorption maximum, while the excited-state coherence generates the node around the fluorescence (or SE) and ESA maxima. The spectral positions of the nodes for 1 (675 nm) and 2 (725 nm) at the early time delay are far from their lowest absorption maxima around 500 nm for 1 and 530 nm for 2 (Figure S10). Notably, the nodal points of the two complexes appear close to the maxima of the SE features in SADS 1 (675 nm for 1 and 750 nm for 750 nm). It has been previously reported in a hydroxypyridyl-birdged Pt dimer that the maximum of the SE signal and the nodal point of the CVWP motion are observed at similar spectral position. Thus, the CVWP motions observed in the entire probe range mostly originate from the excited state PESs.

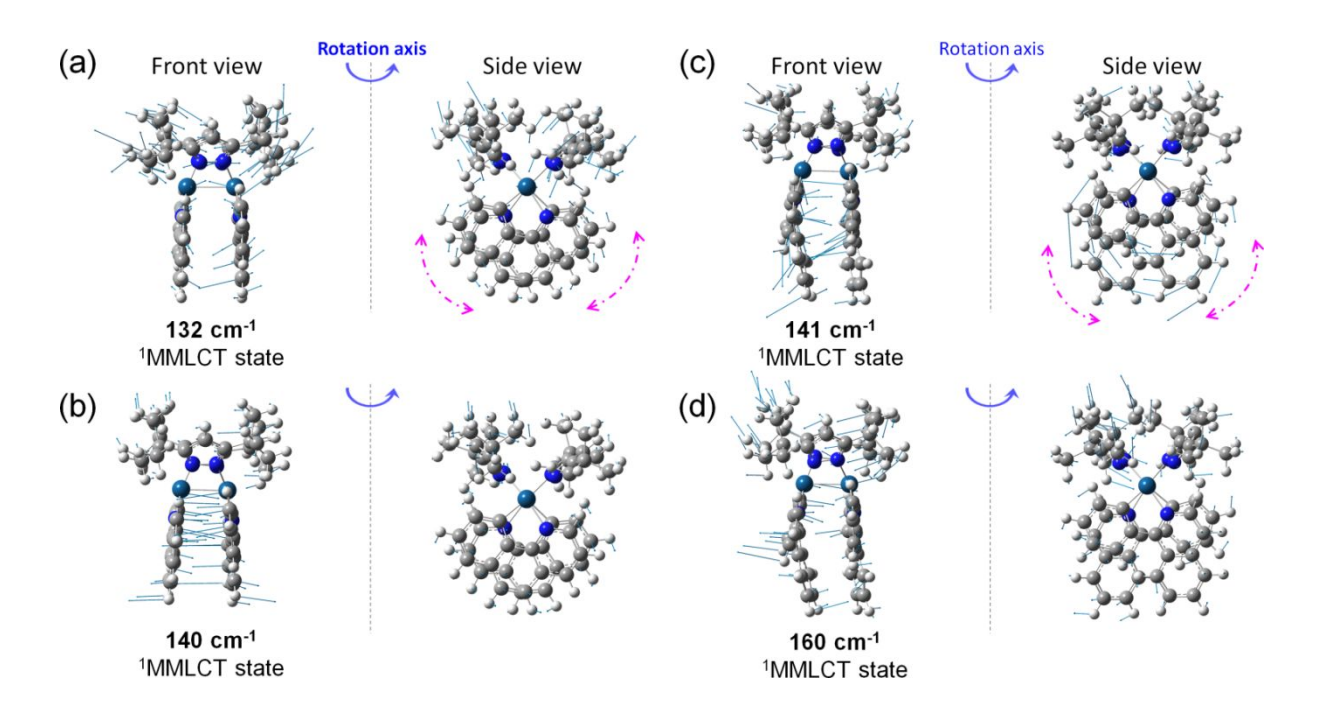


Figure 5. Normal mode analysis results for the optimized structure in the singlet excited-state (¹MMLCT) of Pt-bzq (a, b) and Pt-piq (c, d) of the key vibrational modes. (a) Pt-bzq at 132 cm⁻¹; (b) Pt-bzq at 140 cm⁻¹; (c) Pt-piq at 141 cm⁻¹; and (d) Pt-piq at 160 cm⁻¹. The torsional motions of bzq and piq ligands in the plane perpendicular the axis of Pt—Pt bond are highlighted by the dashed magenta arrows.

To assess the nature of the observed coherent oscillations in 1 and 2, we performed normal mode analyses of their excited-state structures. As presented in Figure 5, the vibrational modes of 132 cm⁻¹ in 1 and 141 cm⁻¹ in 2 are the closest frequencies to the 132 cm⁻¹ and 140 cm⁻¹ identified from TA measurements, respectively. Those vibrational modes feature common collective motions including the torsional motions of the C^N ligand moieties (bzg and piq) in terms of the plane perpendicular to the Pt-Pt bond formed in the excited state. In contrast to the lower frequencies, the vibrations of 140 cm⁻¹ in 1 and 160 cm⁻¹ in 2 are close to the experimentally observed frequencies of 137 cm⁻¹ and 160 cm⁻¹, respectively. Those upshifted vibrations represent the contraction motion of the Pt-Pt bond as well as the collective vibrations of ligand moieties along the axis of the Pt-Pt σ -bond. The previous TA study on 3 (Pt-ppy) reported the contraction motion of the Pt—Pt bond having a frequency of 136 cm⁻¹, assigned as excited-state vibrational coherence. 19 Additionally, the 2-hydroxypyridyl-bridged Pt(II) dimers with bzq ligands also exhibited vibrational motions of the Pt-Pt bond with frequencies ranging from 138 cm⁻¹ to 150 cm⁻¹, assigned as excited-state vibrational coherence generated from the MMLCT transition.²² The absolute values of the observed frequencies in the present study are quantitatively similar to those from these previous observations. 19,21,22 We note that the dephasing dynamics of the coherent oscillations observed in 1 and 2 are highly accelerated relative with respect to the other classes of Pt(II) dimers.

Excited-state ISC Dynamics. The combined results of the electronic population dynamics and the features seen in the coherent oscillations provide comprehensive information on the excited state dynamics of the pyrazolate-bridged Pt(II) dimers. In both 1 and 2, it was observed that the SE feature was quenched with a time constant of ~200 fs during the SADS1 \rightarrow SADS2 transition, which is assigned to the ISC process from the 1 MMLCT state to the 3 MMLCT state and possible internal conversion from the S_{1} state. The excited-state vibrational coherences, originating from the superposition of vibrational manifolds in S_{1} , undergo rapid dephasing dynamics, comparable to the rate of ISC in 1 and precedes that observed in 2. Considering the electronic and dephasing dynamics, we can infer that the transfer of vibrational coherence from the singlet to triplet manifolds (or the intermediate state) observed in previous TA studies, 20,22 is absent in 1 and 2, as there is no CVWP dephasing time lasting for a few picoseconds, which can only occur in the long lived T_{1} state via extremely fast ISC. The normal mode analysis results in Figure 5 show that the lower frequencies (132 cm⁻¹ in 1 and 140 cm⁻¹ in 2) are

consistent with concerted torsional motions of bzg and pig that dephase extremely fast, especially in 2. In contrast, the higher frequency Pt—Pt stretching motions (137 cm⁻¹ in 1 and 160 cm⁻¹ in 2), have slower CVWP dephasing time constant of 261 fs and 102 fs, respectively. This implies that during ISC, the twisting motion of the C^N ligands in the plane perpendicular to the Pt-Pt bond axis predates the Pt-Pt stretching vibrational motions. The disparate CVWP dephasing times observed between 1 and 2 is likely due to CM ligand structural differences. As shown in Figure 5, the bzq ligand is smaller and more rigid compared to the piq ligand having, as shown by the larger structural changes occurring in the excited state (Figure 1) and the larger amplitude motions in the vibrational motions (indicated by the arrow lengths representing the atomic motion vectors in Figure 5). Consequently, the Pt—Pt stretching mode in 2 would not be able to sustain the CVWP motion due to the presence of larger and more floppy piq ligands. The structure of the piq is therefore likely to induce a greater degree of structural constraint due to the expanded benzene ring in the terminal portion of the ligand. Moreover, the pig ligands having a more staggered geometry, as shown in Figure 1, can easily impose significant restrictions on the molecular motion in the ground-state equilibrium structure, due to sterically hindering the bond contraction characteristic of the Pt—Pt interaction. In this regard, photoexcited 2 appear to adopt structural motions circumventing the imposed steric hindrance, such as torsional motions. Thus, efficient redistribution of the vibrational energy along the torsional motion coordinates will be favored and ultimately bring about accelerated dephasing dynamics. This statement is supported by the observation of the delayed dephasing dynamics of ~200-500 fs in the temporal oscillations seen in Pt-ppy. 19 According to the optimized structures of Pt-ppy presented in Figure S11, the S₀-to-S₁ transition brings about a change in the Pt-Pt distance (ΔR_{Pt-Pt}) of 0.213 Å, which is comparable to that seen in 1 and 2. In Pt-ppy, the high degree of structural motion in the ground-state equilibrium structure may induce multiple motions, including the Pt-Pt contraction motion as well as torsional motions in the excited state. Therefore, structural distortions having fewer constraints may influence the efficient dissipation of vibrational energy, resulting in delays of the dephasing dynamics.

In order to examine the possibility of reaction pathways as a function of Pt—Pt distance, the theoretical PESs shown in Figure 6 were calculated by using the intermediate structures reconstructed from linear interpolation between the ground-state and the excited-state geometries. As the Pt—Pt distance decreases, the energy levels of the higher-lying triplet states such as T_2 or T_3 are approaching those of lowest singlet excited state (S_1) and then they become

crossed near a Pt-Pt distance of 2.76 Å. This crossing point might facilitate rapid ISC toward the formation of the relaxed lowest triplet state (3MMLCT) in view of the contractional motion of the Pt-Pt bond. However, the conical intersections between S₁ and T₂ or T₃ are simply too far away from the Franck-Condon region along the Pt-Pt distance coordinate. Thus, they are unlikely to present extremely fast ISC pathways, such as $S_1 \rightarrow T_2(T_3) \rightarrow T_1$ as observed in related Pt dimers in a previous study.⁵¹ Instead, the theoretical results provided here for the PESs imply that only a single ISC pathway, namely $S_1 \rightarrow T_1$, is feasible for 1 and 2. Thus, the CVWP motions for both 1 and 2 only take place while they are in the S₁ state, but diphase as they traverse through ISC to the T₁ state. In addition, we note that the energy gaps between the S₁ and S_0 states in 1 is much larger than that in 2 by approximately 0.5 eV as shown in Figure 6. Consequently, the internal conversion (IC) process from S₁ to S₀ should be more feasible in 2 with respect to 1, opening an additional channel for quenching the S_1 state, resulting in a weaker SE signal and an accelerated CVWP dephasing time. In this study, we successfully captured the excited-state ISC dynamics focusing on the electronic dynamics of the initially populated singlet excited state and the behaviors of vibrational coherences with its dephasing dynamics. Nevertheless, additional studies employing femtosecond impulsive stimulated Raman spectroscopy (ISRS)^{52,53} or femtosecond diffuse X-ray scattering^{54,55} will be required to map out the entire conformational dynamics profiles of 1 and 2. In addition, the existence of offresonant modes of neat solvent added the complexity of the interpretation for the observed vibrational modes with the fast dephasing dynamics. In this regard, the solvent-dependence experiment will be an optimal way to separate the pure on-resonant modes from the observed ones. However, the pyrazolate-bridged Pt(II) dimers have the extremely low solubility in several common organic solvents except THF, which hinders the further study about the solvent effect. Thus, how the off-resonant Raman modes of solvent interplay with the onresonant modes of solute should be investigated by the future additional study. We believe that our future approach based on the next-generation Pt-complexes with the structurally modified ligands can surely contribute toward addressing this.

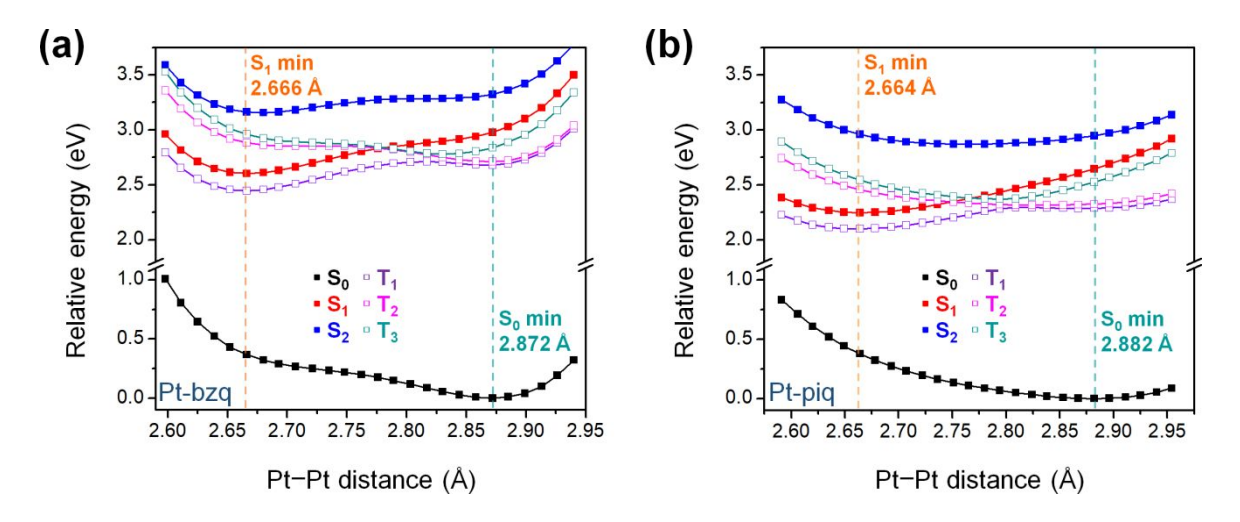


Figure 6. Calculated potential energy surfaces (PESs) as a function of Pt-Pt distance. PESs of (a) Pt-bzq and (b) Pt-piq. The filled squares indicate the energies of singly excited states, and the open squares indicate the energies of triplet excited states. For clarity, the Pt—Pt distances in the optimized structures of ground (S_0) and first singly excited states (S_1) are denoted as the color-coded dashed lines.

Conclusions

In this study, we directly detected the ultrafast dynamics of pyrazolate-bridged Pt(II) dimers, including the coherent vibrational wavepacket motions on the excited-state potential energy surface through the intersystem crossing trajectory. Our results show that upon excitation into the lowest ¹MMLCT transitions of Pt-bzq and -piq complexes, the ISC processes from the emissive singlet (S₁) to the ³MMLCT state commonly occur with the time constant of ~200 fs and subsequently, the higher-lying vibrational manifolds of the triplet excited states undergo relaxation within ~2 ps. The coherent oscillations associated with the excited-state vibrational motions appeared near the experimental time origin and then were dephased, accompanying the quenching of the SE feature during the ISC dynamics. Results from the normal mode analyses suggested that the lower frequency of 132 cm⁻¹ in 1 and 140 cm⁻¹ in 2 were related to the concerted torsional motions of the CM ligand moieties in the plane perpendicular to the axis of Pt—Pt bond. In contrast, the higher frequency of 137 cm⁻¹ in 1 and 160 cm⁻¹ in 2 were associated with the vibrational motions along the Pt—Pt bond formed in the excited state. The dynamic behavior of coherent wavepackets showed rapid dephasing, which is comparable to the rate of the ISC process in 1 and precedes that in 2. More importantly, this study revealed

two important roles that the CM ligands play in modulating the excited state trajectories. First, a more π -conjugated CM ligand serves to lower the LUMO π^* energy, and consequently the energy gap between S_1 and S_0 , resulting in a higher rate of internal conversion and SE emission quenching. Second, larger and less structurally rigid CM ligands increase their moment of inertia thereby hindering the CVWP motion characteristic of the Pt-Pt stretching mode, resulting in faster dephasing. The combined results should be considered as a means for coherent control of photoinduced charge transfer processes in TMCs through structural engineering. Such photoinduced control of charge transfer dynamics will enable the conversion of light energy into chemical energy through leveraging quantum coherence phenomena.

Associated Content

Supporting Information

The supporting information is available free of charge on the xxx website at DOI: XXX.

Details on the synthesis and structural characterization of 1 and 2; global kinetic analysis and FT procedure; steady-state spectroscopic results; temporal profile related to the instrumental response function; TA data for the wide time window; off-resonant transient signal acquired by the neat THF solvent; two-dimensional residual maps; results from the normal mode analyses; optimized structure of 3; NTOs from the TD-DFT calculations; Cartesian coordinates for optimized geometries of Pt(II) dimers. (PDF)

Author Information

Corresponding Author

*E-mail: lchen@anl.gov, l-chen@northwestern.edu (L.X.C); fncastel@ncsu.edu (F.N.C); xsli@uw.edu (X.L).

Notes

The authors declare no competing financial interest.

†Present address: Department of Chemistry, Mokpo National University, Muan-gun, Jeollanam-do, 58554, Republic of Korea (T.W.K)

Acknowledgements

This work has been supported by the National Science Foundation (Grant CHE-1955806 to L.X.C. and Grant CHE-1955795 to F.N.C.). The computational work and T.W.K., P.K., and L.X.C. is supported in part by the Ultrafast Initiative of the U.S. Department of Energy, Office of Science, Office of Basic Energy Sciences, through Argonne National Laboratory under Contract DE-AC02-06CH11357. The development of the computational method for simulating excited-state dynamics is supported by the National Science Foundation (Grant CHE1856210 to X.L.).

References

- **(1)** Esswein, A. J.; Nocera, D. G.: Hydrogen production by molecular photocatalysis. Chem. Rev. 2007, 107, 4022-4047.
- Xie, J.; Li, C.; Zhou, Q.; Wang, W.; Hou, Y.; Zhang, B.; Wang, X.: Large improvement in the catalytic activity due to small changes in the diimine ligands: new mechanistic insight into the dirhodium(II,II) complex-based photocatalytic H2 production. Inorg. Chem. 2012, 51, 6376-6384.
- Li, Z.; Leed, N. A.; Dickson-Karn, N. M.; Dunbar, K. R.; Turro, C.: Directional charge transfer and highly reducing and oxidizing excited states of new dirhodium(II,II) complexes: potential applications in solar energy conversion. Chem. Sci. 2014, 5, 727-737.
- **(4)** Evans, R. C.; Douglas, P.; Winscom, C. J.: Coordination complexes exhibiting room-temperature phosphorescence: Evaluation of their suitability as triplet emitters in organic light emitting diodes. Coord. Chem. Rev. 2006, 250, 2093-2126.
- Ma, B.; Djurovich, P. I.; Garon, S.; Alleyne, B.; Thompson, M. E.: Platinum Binuclear Complexes as Phosphorescent Dopants for Monochromatic and White Organic Light-Emitting Diodes. Adv. Funct. Mat. 2006, 16, 2438-2446.
- Liu, Z.; He, W.; Guo, Z.: Metal coordination in photoluminescent sensing. (6) Chem. Soc. Rev. 2013, 42, 1568-1600.
- Pal, S.; Chatterjee, N.; Bharadwaj, P. K.: Selectively sensing first-row (7) transition metal ions through fluorescence enhancement. RSC Adv. 2014, 4, 26585-26620.
- Ho, C.-L.; Wong, W.-Y.; Yao, B.; Xie, Z.; Wang, L.; Lin, Z.: Synthesis, characterization, photophysics and electrophosphorescent applications of phosphorescent platinum cyclometalated complexes with 9-arylcarbazole moieties. J. Organomet. Chem. 2009, 694, 2735-2749.
- (9) Roundhill, D. M.; Gray, H. B.; Che, C. M.: Pyrophosphito-bridged diplatinum chemistry. Acc. Chem. Res. 1989, 22, 55-61.
- Durrell, A. C.; Keller, G. E.; Lam, Y. C.; Sykora, J.; Vlcek, A., Jr.; Gray, H. B.: Structural control of 1A2u-to-3A2u intersystem crossing in diplatinum(II,II) complexes. J. Am. Chem. Soc. 2012, 134, 14201-14207.
- Chen, W.-C.; Chou, P.-T.; Cheng, Y.-C.: Low Internal Reorganization Energy (11)of the Metal–Metal-to-Ligand Charge Transfer Emission in Dimeric Pt(II) Complexes. J. Phys. Chem. C 2019, 123, 10225-10236.
- Chakraborty, A.; Deaton, J. C.; Haefele, A.; Castellano, F. N.: Charge-Transfer and Ligand-Localized Photophysics in Luminescent Cyclometalated Pyrazolate-Bridged Dinuclear Platinum(II) Complexes. *Organometallics* **2013**, *32*, 3819-3829.
- Rachford, A. A.; Castellano, F. N.: Thermochromic absorption and photoluminescence in [Pt(ppy)(mu-Ph2pz)]2. *Inorg. Chem.* **2009**, 48, 10865-10867.

- Saito, K.; Nakao, Y.; Sakaki, S.: Theoretical study of pyrazolate-bridged dinuclear platinum(II) complexes: interesting potential energy curve of the lowest energy triplet excited state and phosphorescence spectra. *Inorg. Chem.* **2008**, 47, 4329-4337.
- Brown-Xu, S. E.; Kelley, M. S.; Fransted, K. A.; Chakraborty, A.; Schatz, G. C.; Castellano, F. N.; Chen, L. X.: Tunable Excited-State Properties and Dynamics as a Function of Pt-Pt Distance in Pyrazolate-Bridged Pt(II) Dimers. J. Phys. Chem. A 2016, 120, 543-550.
- Weingartz, N. P.; Mara, M. W.; Roy, S.; Hong, J.; Chakraborty, A.; Brown-(16)Xu, S. E.; Phelan, B. T.; Castellano, F. N.; Chen, L. X.: Excited-State Bond Contraction and Charge Migration in a Platinum Dimer Complex Characterized by X-ray and Optical Transient Absorption Spectroscopy. J. Phys. Chem. A **2021**, 125, 8891-8898.
- Cho, S.; Mara, M. W.; Wang, X.; Lockard, J. V.; Rachford, A. A.; Castellano, F. N.; Chen, L. X.: Coherence in metal-metal-to-ligand-charge-transfer excited states of a dimetallic complex investigated by ultrafast transient absorption anisotropy. J. Phys. Chem. A **2011**, 115, 3990-3996.
- (18)Haldrup, K., Dohn, A. O., Shelby, M. L., Mara, M. W., Stickrath, A. B., Harpham, M. R., Huang, J., Zhang, X., Moller, K. B., Chakraborty, A.et al.: Butterfly Deformation Modes in a Photoexcited Pyrazolate-Bridged Pt Complex Measured by Time-Resolved X-Ray Scattering in Solution. J. Phys. Chem. A 2016, 120, 7475-7483.
- Mewes, L.; Ingle, R. A.; Megow, S.; Bohnke, H.; Baranoff, E.; Temps, F.; Chergui, M.: Ultrafast Intersystem Crossing and Structural Dynamics of [Pt(ppy)(mu-(t)Bu2pz)]2. Inorg. Chem. 2020, 59, 14643-14653.
- Monni, R.; Capano, G.; Aubock, G.; Gray, H. B.; Vlcek, A.; Tavernelli, I.; Chergui, M.: Vibrational coherence transfer in the ultrafast intersystem crossing of a diplatinum complex in solution. Proc. Natl. Acad. Sci. USA 2018, 115, E6396-E6403.
- Kim, P.; Kelly, M. S.; Chakraborty, A.; Wong, N. L.; Van Duyne, R. P.; Schatz, G. C.; Castellano, F. N.; Chen, L. X.: Coherent Vibrational Wavepacket Dynamics in Platinum(II) Dimers and Their Implications. J. Phys. Chem. C 2018, 122, 14195-14204.
- Kim, P.; Valentine, A. J. S.; Roy, S.; Mills, A. W.; Chakraborty, A.; Castellano, (22)F. N.; Li, X.; Chen, L. X.: Ultrafast Excited-State Dynamics of Photoluminescent Pt(II) Dimers Probed by a Coherent Vibrational Wavepacket. J. Phys. Chem. Lett. 2021, 12, 6794-6803.
- Radler, J. J.; Lingerfelt, D. B.; Castellano, F. N.; Chen, L. X.; Li, X.; Role of (23)Vibrational Dynamics on Excited-State Electronic Coherence in a Binuclear Platinum Complex. J. Phys. Chem. A 2018, 122, 5071-5077.
- Lingerfelt, D. B.; Lestrange, P. J.; Radler, J. J.; Brown-Xu, S. E.; Kim, P.; Castellano, F. N.; Chen, L. X.; Li, X.; Can Excited State Electronic Coherence Be Tuned via Molecular Structural Modification? A First-Principles Quantum Electronic Dynamics Study of Pyrazolate-Bridged Pt(II) Dimers. J. Phys. Chem. A 2017, 121, 1932-1939.
- Liedy, F.; Eng, J.; McNab, R.; Inglis, R.; Penfold, T. J.; Brechin, E. K.; Johansson, J. O.: Vibrational coherences in manganese single-molecule magnets after ultrafast photoexcitation. Nat. Chem. 2020, 12, 452-458.
- Schrauben, J. N.; Dillman, K. L.; Beck, W. F.; McCusker, J. K.: Vibrational (26)coherence in the excited state dynamics of Cr(acac)3: probing the reaction coordinate for ultrafast intersystem crossing. Chem. Sci. 2010, 1, 405-410.
- Lemke, H. T.; Kjaer, K. S.; Hartsock, R.; van Driel, T. B.; Chollet, M.; (27)Glownia, J. M.; Song, S.; Zhu, D.; Pace, E.; Matar, S. F.; et al. Coherent structural trapping through wave packet dispersion during photoinduced spin state switching. *Nat. Commun.* **2017**, 8, 15342.
 - Paulus, B. C.; Adelman, S. L.; Jamula, L. L.; McCusker, J. K.: Leveraging (28)

excited-state coherence for synthetic control of ultrafast dynamics. *Nature* **2020**, *582*, 214-218.

- Halpin, A.; Johnson, P. J.; Tempelaar, R.; Murphy, R. S.; Knoester, J.; Jansen, T. L.; Miller, R. J.: Two-dimensional spectroscopy of a molecular dimer unveils the effects of vibronic coupling on exciton coherences. Nat. Chem. 2014, 6, 196-201.
- Turner, D. B.; Wilk, K. E.; Curmi, P. M. G.; Scholes, G. D.: Comparison of Electronic and Vibrational Coherence Measured by Two-Dimensional Electronic Spectroscopy. J. Phys. Chem. Lett. 2011, 2, 1904-1911.
- Cheng, Y. C.; Fleming, G. R.: Coherence quantum beats in two-dimensional (31)electronic spectroscopy. J. Phys. Chem. A 2008, 112, 4254-4260.
- Hayes, D.; Griffin, G. B.; Engel, G. S.: Engineering coherence among excited states in synthetic heterodimer systems. Science 2013, 340, 1431-1434.
- Fuller, F. D.; Pan, J.; Gelzinis, A.; Butkus, V.; Senlik, S. S.; Wilcox, D. E.; Yocum, C. F.; Valkunas, L.; Abramavicius, D.; Ogilvie, J. P.: Vibronic coherence in oxygenic photosynthesis. Nat. Chem. 2014, 6, 706-711.
- Gaynor, J. D.; Sandwisch, J.; Khalil, M.: Vibronic coherence evolution in multidimensional ultrafast photochemical processes. Nat. Commun. 2019, 10, 5621.
- Frisch, M. J.; Trucks, G. W.; Schlegel, H. B.; Scuseria, G. E.; Robb, M. A.; (35)Cheeseman, J. R.; Scalmani, G.; Barone, V.; Petersson, G. A.; Nakatsuji, H.; et al. Gaussian 16 Rev. B.01. Wallingford, CT, 2016.
- Atkins, A. J.; Talotta, F.; Freitag, L.; Boggio-Pasqua, M.; Gonzalez, L.: Assessing Excited State Energy Gaps with Time-Dependent Density Functional Theory on Ru(II) Complexes. J. Chem. Theory Comput. 2017, 13, 4123-4145.
- Chai, J. D.; Head-Gordon, M.: Systematic optimization of long-range corrected hybrid density functionals. J. Chem. Phys. 2008, 128, 084106.
- Latouche, C.; Skouteris, D.; Palazzetti, F.; Barone, V.: TD-DFT Benchmark on Inorganic Pt(II) and Ir(III) Complexes, J. Chem. Theory Comput. 2015, 11, 3281-3289.
 - Martins, R. L.: Natural transition orbitals. J. Chem. Phys. 2003, 118, 4775. (39)
- (40)Barzegar-Kiadehi, S. R.; Golbon Haghighi, M.; Jamshidi, M.; Notash, B.: Influence of the Diphosphine Coordination Mode on the Structural and Optical Properties of Cyclometalated Platinum(II) Complexes: An Experimental and Theoretical Study on Intramolecular Pt...Pt and pi...pi Interactions. *Inorg. Chem.* **2018**, *57*, 5060-5073.
- Kim, T. W.; Jun, S.; Ha, Y.; Yadav, R. K.; Kumar, A.; Yoo, C. Y.; Oh, I.; Lim, (41)H. K.; Shin, J. W.; Ryoo, R.; et al. Ultrafast charge transfer coupled with lattice phonons in two-dimensional covalent organic frameworks. *Nat. Commun.* **2019**, *10*, 1873.
- Voehringer, P.; Scherer, N. F.: Transient Grating Optical Heterodyne Detected (42)Impulsive Stimulated Raman Scattering in Simple Liquids. J. Phys. Chem. 1995, 99, 2684-2695.
- Shuvell, H. F.; Southby, M. C.: Infrared and Raman spectra of tetrahydrofuran (43)hydroperoxide. Vib. Spectrosc. 1997, 15, 137-146.
- (44)Dean, J. C.; Rafig, S.; Oblinsky, D. G.; Cassette, E.; Jumper, C. C.; Scholes, G. D.: Broadband Transient Absorption and Two-Dimensional Electronic Spectroscopy of Methylene Blue. J. Phys. Chem. A 2015, 119, 9098-9108.
- Ikuta, M.; Yuasa, Y.; Kumar, T.; Hiroo, M.; Kobayashi, T.: Phase analysis of (45)vibrational wave packets in the ground and excited states in polydiacetylene. Phys. Rev. B 2004, 70, 214301.
- Dhar, L.; Rogers, J. A.; Nelson, K. A.: Time-resolved vibrational spectroscopy (46)in the impulsive limit. Chem. Rev. 1994, 94, 157-193.
- McClure, S. D.; Turner, D. B.; Arpin, P. C.; Mirkovic, T.; Scholes, G. D.: Coherent oscillations in the PC577 cryptophyte antenna occur in the excited electronic state. J.

- Phys. Chem. B 2014, 118, 1296-308.
- (48) Cina, J. A.; Kovac, P. A.; Jumper, C. C.; Dean, J. C.; Scholes, G. D.: Ultrafast transient absorption revisited: Phase-flips, spectral fingers, and other dynamical features. *J. Chem. Phys.* **2016**, *144*, 175102.
- (49) Rafiq, S.; Scholes, G. D.: Slow Intramolecular Vibrational Relaxation Leads to Long-Lived Excited-State Wavepackets. *J. Phys. Chem. A* **2016**, *120*, 6792-9.
- (50) Kim, P.; Valentine, A. J. S.; Roy, S.; Mills, A. W.; Castellano, F. N.; Li, X.; Chen, L. X.: Ultrafast branching in intersystem crossing dynamics revealed by coherent vibrational wavepacket motions in a bimetallic Pt(II) complex. **2022**, *10.1039/D2FD00009A*.
- (51) Kim, P.; Valentine, A. J. S.; Roy, S.; Mills, A. W.; Chakraborty, A.; Castellano, F. N.; Li, X.; Chen, L. X.: Ultrafast Excited-State Dynamics of Photoluminescent Pt(II) Dimers Probed by a Coherent Vibrational Wavepacket. *J. Phys. Chem. Lett.* **2021**, *12*, 6794–6803.
- (52) Liebel, M.; Schnedermann, C.; Wende, T.; Kukura, P.: Principles and Applications of Broadband Impulsive Vibrational Spectroscopy. *J. Phys. Chem. A* **2015**, *119*, 9506-9517.
- (53) Kuramochi, H.; Takeuchi, S.; Tahara, T.: Femtosecond time-resolved impulsive stimulated Raman spectroscopy using sub-7-fs pulses: Apparatus and applications. *Rev. Sci. Instrum.* **2016**, *87*, 043107.
- (54) Kim, K. H.; Kim, J. G.; Nozawa, S.; Sato, T.; Oang, K. Y.; Kim, T. W.; Ki, H.; Jo, J.; Park, S.; Song, C.; *et al.* Direct observation of bond formation in solution with femtosecond X-ray scattering. *Nature* **2015**, *518*, 385-389.
- (55) Haldrup, K.; Levi, G.; Biasin, E.; Vester, P.; Laursen, M. G.; Beyer, F.; Kjaer, K. S.; van Driel, T. B.; Harlang, T.; Dohn, A. O.; *et al.* Ultrafast X-Ray Scattering Measurements of Coherent Structural Dynamics on the Ground-State Potential Energy Surface of a Diplatinum Molecule. *Phys. Rev. Lett.* **2019**, *122*, 063001.

TOC Graphic

